Anal Bioanal Chem (2003) 376 : 608–617
DOI 10.1007/s00216-003-1904-3

SPECIAL ISSUE PAPER

Norbert Stribeck

Nanostructure evolution studies of bulk polymer materials with synchrotron radiation: progress in method development

Received: 2 December 2002 / Revised: 5 March 2003 / Accepted: 10 March 2003 / Published online: 11 June 2003

Abstract The prospects of a modern analysis of nanostructure evolution during the processing of polymer materials by means of scattering from synchrotron radiation are demonstrated in examples. The beam sources have gained stability, shortages are located in beamline setups and in method development for the quantitative analysis of voluminous data sets.By using the proposed multidimensional chord distribution function (CDF) analysis method, nanostructure information from small-angle X-ray scattering (SAXS) data are extracted and visualised. The method can be automated if the beamline setup is able to deliver a full data set with simple constraints. In this case even a simultaneous data evaluation is possible (while one pattern is accumulated, the previous one is analysed). The advantages of the method are demonstrated in a study of the straining of a thermoplastic elastomer. The possibilities of an automated analysis are demonstrated in an investigation of the crystallisation behaviour of high-pressure injection-moulded polyethylene (HPIM-PE). The achievable results of nanostructure analysis of polymer materials are discussed. It is shown that the time-resolved SAXS of polymer materials studied during a transformation and analysed by the CDF method is not just a powerful tool to investigate the relationship between structure and properties of materials; the information that can be gained concerning the processes that control nanostructure evolution is equally important. In the future the enlightenment of such relationships may help to tailor polymer materials with respect to their properties and, beyond that, to improve assessments concerning their aging.

Keywords Synchrotron radiation · Instrument setup · SAXS · Polymer materials · Evaluation method · Automation

N. Stribeck (✉)
Institute of Technical and Macromolecular Chemistry,
University of Hamburg,
Bundesstrasse 45, 20146 Hamburg, Germany
e-mail: Norbert.Stribeck@desy.de

Introduction

In many fields of materials science synchrotron radiation is utilised to study processes. With polymer materials such processes may be crystallisation or the application of mechanical load that cause the nanostructure of hard and soft domains to (re)develop. During service of a polymer part, transition processes frequently cannot be avoided. Thus it is essential to understand the driving forces of this evolution not only because of its impact on the production of tailored materials, but also in order to assess the lifetime of such parts.

Progress in synchrotron radiation research was for a long time mainly based on the development of dedicated and stable synchrotron sources. In this period, data that were recorded were generally not suitable for a quantitative evaluation even if the measuring intervals were chosen to be rather long. Nevertheless, the scientific community has shown that even such moderate data sets can help to promote notions concerning nanostructure and its evolution, although the significance of evidence gathered this way is generally not very high.

As far as up-to-date progress of synchrotron radiation research is concerned, two major trends can be observed. Increasing stability, brilliance, and decreasing beam cross section allow, on the one hand, one to perform more and more cutting edge experiments. Necessarily their data quality remains moderate. Evaluation will most probably be restricted to an interpretation of the data. This approach is paralleled by the ambition to profit from the increasing beam quality by increasing the data quality. In this second case both the problems of appropriate data evaluation methods and the handling of huge amounts of data have to be solved. It should be noted that considerations undertaken so far have some implications concerning the design of a synchrotron beam device. Inappropriate design may block the option to automatically evaluate the collected data.

It is to be noted that different communities rank the scientific value of both approaches differently. Cutting edge experiments themselves carry the charms of absolute nov-

elty. On the other hand, high-precision data shall result in proper evidence after data evaluation. In order to achieve this goal we require standardised methods to be developed.

In several fields of materials science the importance of method development has been recognised and supported early. The great success of protein crystallography, for example, is mainly based on the development and standardisation of methods for the evaluation of synchrotron radiation data [1] that resulted in evidence of unparalleled precision concerning crystal structure. Similar awareness is still low in the field of polymer materials science, at least as far as promotion and funding of such projects is concerned. Thus I use this opportunity to point out perspectives of a standardised methodical evaluation based on my own work in the field of small-angle X-ray scattering (SAXS).

Similar to the field of crystallography, where the change from a powder diagram to single-crystal data is associated with a considerable reduction of ambiguity, the change from isotropic scattering curves to anisotropic scattering patterns is associated with a corresponding gain of structural information. Thus scattering curves, in general, are analysed after resorting to a chosen model of the nanostructure (stacks of lamellae [2, 3, 4, 5], spherical or cylindrical vesicles [6], uncorrelated particles with a constant electron density [7, 8]). On the other hand, when studying anisotropic scattering patterns it is quite frequently possible to draw conclusions on the nanostructure without need to resort to a model.

Progress in method

Overview

Whenever scattering methods are utilised, data is recorded in reciprocal space. From this data structural information in physical space can be gained. Each effect, which in the scattering pattern is manifested as a slowly varying function, can be assigned to low spatial frequencies in physical space. Counting statistics, on the other hand, is most clearly apparent at high spatial frequencies. Thus the accessible structural information of a scattering pattern is contained in a spatial frequency band between background frequencies and high-frequency noise. If an interpretation of the scattering pattern in reciprocal space is not accepted, a (multidimensional) correlation function [4, 9], an interface distribution function (IDF) [5, 10, 11] or a chord distribution [3, 12] may be computed and analysed. According to the previous considerations, such an image is computed in three automatable steps: (I) Proper transformation of the scattering pattern, (II) band-pass filtering and (III) Fourier transformation. Thus now the choice of filter characteristics must be discussed and takes the place of a discussion of deviations from the ideal multiphase model [13]. Given the new paradigm, the effect of smoothing the scattering pattern by a band-pass filter on the morphology gets a novel meaning. The upper edge of the filter defines a distance in real space, beyond which no information on correlations among domains can be retrieved. Hence the main effect of noise reduction by prolonged exposure is the increase of information on long-range order.

Definitions

Let $I(\mathbf{s})$ be the observed small-angle scattering (SAS) intensity. The magnitude of the scattering vector can be defined by $|\mathbf{s}|=(2/\lambda)\sin\theta$ where λ is the wavelength of radiation and 2θ is the scattering angle. Common notations will be used for both the case of isotropic scattering patterns by writing $I(\mathbf{s})=I(s)$ with $s=|\mathbf{s}|$, and for the case of a scattering pattern with fibre symmetry, $I(\mathbf{s})=I(s_{12}, s_3)$ with $s_{12}=\sqrt{s_1^2+s_2^2}$ and the direction of s_3 defining the symmetry axis of the pattern.

For the two cases mentioned one frequently can guarantee that the recorded information on the structure is complete. In the isotropic case the complete information of SAS is contained in a curve. In the case of fibre symmetry the complete information of SAS is in a two-dimensional (2D) pattern, which can be recorded by using a 2D detector.

Intensity projection onto a plane

If the scattering pattern is already complete in a subspace of the 3D reciprocal space, the suitable projection [14, 15, 16, 17] has to be carried out before the following 1D or 2D Fourier transformation. In classical methods special Fourier kernels are employed, which comprise the projection implicitly. For the data evaluation of scattering "images" with fibre symmetry it is convenient to utilise commercial standard software for image processing like *pvwave* [18], *IDL* or *Matlab* to carry out the necessary projection

$$I_P(s_1, s_3) = \{I(s_{12}, s_3)\}(s_1, s_3) = \int I(s_{12}, s_3\, ds_2) \qquad (1)$$

the 2D Fourier transformation $\mathcal{F}^2(I_P)(r_{12},r_3)=P(r_{12},r_3)$ of which is known as the 2D (electron-) density correlation function [9] in cylindrical coordinates. Let us consider a correlation function computed from ideal model data and turned into a 2D digital image. Then, anticipating the next subsection and resorting to the paradigms of the field of digital image processing, the generalised chord distribution can be computed by convolution with the digital Laplacian operator [19, 20]

$$L_d = \begin{pmatrix} 0 & -1 & 0 \\ -1 & 4 & -1 \\ 0 & -1 & 0 \end{pmatrix}$$

A generalised chord distribution

In the case of isotropic data the features of the nanostructure can be visualised much more clearly in a chord distri-

bution function (CDF) [12] or interface distribution (IDF) [5] than in a correlation function. The reason is that both the CDF and the IDF show an edge-enhanced view of the nanostructure, resting on the concept of a multiphase structure of domains. Now the question arises as to how the one-dimensional concepts of the CDF and the IDF can be generalised for the case of multidimensional scattering data from multiphase systems. Here only the approach, which has proven its feasibility for the evaluation of experimental data, is outlined.

The autocorrelation of the gradient of the density distribution can be defined as a chord distribution $z(\mathbf{r})=(\nabla\rho(\mathbf{r}))^{*2}$ for any multidimensional case. It is equivalent to the Laplacian $\Delta P(\mathbf{r})$ of the correlation function and can be computed from the multidimensional Fourier transformation of the scattering intensity $I(\mathbf{s})$ after multiplication by $4\pi^2 s^2$. For samples with fibre symmetry we start from the projected intensity (I_p) and obtain

$$I_L(s_1, s_3) = 4\pi^2 s^2 I_p(s_{1,} s_3) \tag{2}$$

with $s^2 = \sqrt{s_1^2 + s_3^2}$ in this context.

In the next evaluation step the nonideal character of the studied multiphase structure has to be considered. In the classical methods [5, 21, 22] this is accomplished by subtraction of several slowly varying backgrounds. These backgrounds are well justified from physical reason, but difficult to separate. The result of this operation is an interference function $G(\mathbf{s})$, which shall become subject to a Fourier transformation. Since our interest is not the study of the nonideal character but information on shape and arrangement of the nanometre-size domains, the composite slowly varying background in the SAS image is considered a parasitic effect which is to be eliminated. Obviously a suitable background can be extracted from the SAS pattern itself by computing the low-pass-filtered pattern, $f_{\lambda,r_c}(I_L(\mathbf{s}))$. Its subtraction reduces the central singularity in the Fourier transformation of $I_L(\mathbf{s})$. Hence an adapted interference function $G(\mathbf{s})$

$$G(\mathbf{s}) = I_L(\mathbf{s}) - f_{\lambda,r_c}(I_L(\mathbf{s})) \tag{3}$$

is defined based on a low-pass filter operator f_{λ,r_c} with a cut-off frequency r_c. Filter parameter variation shows that the final CDF is altered marginally only, as long as a filter with smooth frequency response is chosen and the cut-off frequency is kept low. For the commonly used Butterworth filter this means that a low order has to be chosen in order not to imprint artefacts resulting from discontinuities of the filter response function. A first-order Butterworth filter

$$f_{\lambda,r_c}(I_L(\mathrm{s})) = \mathcal{F}^{-1}\left(\mathcal{F}(I_L(\mathrm{s}))(\mathrm{r})\,\frac{1}{(1+r/r_c)^2}\right) \tag{4}$$

has proved feasible in many fields of research ($r=|\mathbf{r}|$). Here $\mathcal{F}$ designates the multidimensional Fourier transformation.

Background subtraction by spatial frequency filtering is not only suitable for the multidimensional case, but also it can be carried out automatically. Moreover, it can be applied iteratively "until the integral of the resulting interference function is vanishing" (i.e. until a central singularity of $z(\mathbf{r})$ is vanishing). Iterative background elimination has proven to be essential for the nanostructure analysis of a class of polymers with rough surfaces of the hard and soft domains (polyurethanes, polyetheresters). For polymers with smooth domain surfaces there is no need to iterate background elimination.

Increasing trust in the iterative elimination grows from the comparison of structural data extracted from the corresponding CDFs and the features of the raw scattering patterns. It must be admitted that CDFs not iterated may show such a high level of roughness that there is no chance to interpret or analyse these real space data. Only after the iterative procedure we find the expected information on domains and their mutual arrangement. The basic result of comparing the features of the scattering pattern with the noniterated and the iterated CDFs shows that iteration of the CDF is emphasising the harmonic fraction of the nanodomain structure in a similar manner as human perception is emphasising it when raw scattering patterns are interpreted.

Noise filter

Filtering of the high-frequency noise is not necessary whenever isotropical or fibre samples with short-range correlated nanostructure are studied and when the original data have been measured with high accuracy (more than 10,000 counts in the maximum). Then the necessary projection serves noise reduction without loss of nanostructure information.

Discrete Fourier transformation

Finally the interference function $G(\mathbf{s})$ or $G_l(\mathbf{s})$ is subject to a discrete Fourier transformation. The result $z(\mathbf{r})=-\mathcal{F}(G(\mathbf{s}))$ is the chord distribution $z(\mathbf{r})$. Starting from the projection $I_P(s_1,s_3)$ of a scattering pattern with fibre symmetry, a 2D Fourier transformation yields the section of $z(r_1,r_3)$ in the (r_1,r_3)-plane. Because of fibre symmetry the equivalence $r_1=r_{12}$ is valid. Thus the complete morphological information concerning size and arrangement of domains is right at hand in the physical space function $z(r_{12},r_3)$ after few evaluation steps (Fig. 1).

Application to isotropic samples

An increasing number of authors utilise the IDF method to interpret the nanostructure inherent to SAXS data by assuming that a lamellar nanostructure is valid for samples that show an isotropic SAXS [17, 23, 24, 25, 26, 27, 28, 29, 30, 31, 32, 33, 34, 35, 36, 37, 38, 39, 40]. Furthermore the volume of data to be analysed is bulging because of an increasing number of time-resolved experiments. Thus there is good reason to define background subtraction in a manner restricting user intervention and allowing

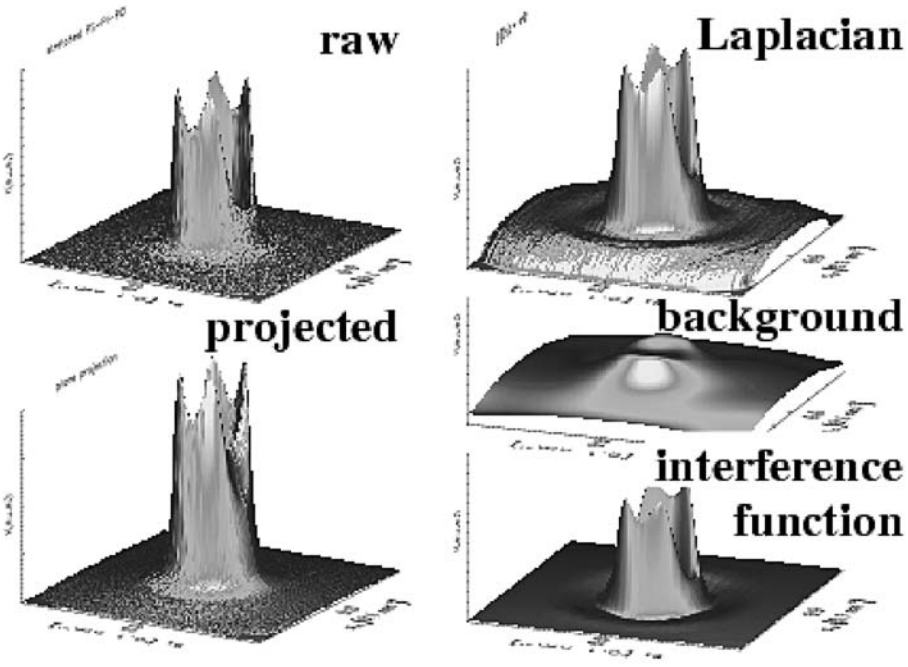

Fig. 1 A SAXS fibre pattern and the evaluation steps leading to an interference function $G(\mathbf{s})$ of the ideal domain nanostructure. The 2D Fourier transformation of $G(\mathbf{s})$ is the sought chord distribution function $z(\mathbf{r})$

for automated processing of series of data [40]. The technique outlined in the preceding subsections for the anisotropic case meets the mentioned requirements and can easily be transformed to the isotropic case as well [41].

Progress in data handling: combining beamline design, image processing and SAXS theory

If variation of nanostructure shall not only be observed but also be evaluated efficiently and completely, several foundations concerning the beamline design should be laid. Although these foundations are theoretically taken for granted, the practical experience of the user shows that a lot of effort has to be undertaken in this field in the future. Scattering patterns must be evaluated precisely and quickly. Valid data must be separated from invalid pixels in each pattern, and the instrumental variations among the patterns from the same series should be simple and well documented.

Thus extensive cloudings of the patterns should be avoided (e.g. by shades of wires winding through the pattern) that may seriously obstruct an automatic determination of valid regions. Similarly unsuitable are instable detectors (Vidicon) or image plate detectors that must be removed for readout. Patterns obtained from such detectors must be evaluated individually by hand. Moreover, the intrinsic uncertainty resulting from such detectors can only be tolerated if the samples are strong scatterers. Thus a self-calibrating, two-dimensional CCD detector with 1,024×1,024 pixels appears to be the minimum requirement for the SAXS. High-resolution detectors (from 4,096×4,096 pixels) may help to simultaneously collect SAXS and MAXS ("middle-angle X-ray scattering") data or even to cover the whole range from SAXS to wide-angle X-ray scattering (WAXS) – if the beamline optics are sufficiently focusing over a wide range of sample-to-detector distances.

If, on the other hand, the interesting angular range cannot be recorded simultaneously, a reproducible, automatic swap between different adjustments of the beamline should be aimed at. For this purpose the detector ought to be traversable automatically along the optical bench with the size of the primary beam stop adapted automatically [42].

Each of these adjustments is characterised by one empty scattering pattern, one mask pattern that is describing the invalid regions in each pattern, information on the position of the centre of the pattern and its orientation, the beam intensity and specific parameters of the experiment. If the setup is completely described by parameter values automatically logged during the experiment as well as by masks and test patterns, the evaluation of the data may be performed during measurement almost in real-time (while an image is exposed, the preceding pattern is evaluated).

To establish such rapid and automated evaluation it is not sufficient to understand scattering theory. It is also important to understand and to implement established methods and paradigms of digital image processing (e.g. erode, closing, opening, region of interest (ROI) operations) [43]. For this purpose and for rapid prototyping there are some commercial (*pv-wave*, *IDL*, *Matlab*) and free (*octave*, *SciLab*, *ImageJ*) software engineering platforms.

Progress in analysis of scattering patterns

In many studies the scattering pattern is interpreted. For this purpose Bragg's law and similar simple notions that describe the reciprocal relationship between pattern and nanostructure are commonly utilised. On this basis cartoons of a probable nanostructure are generated and re-

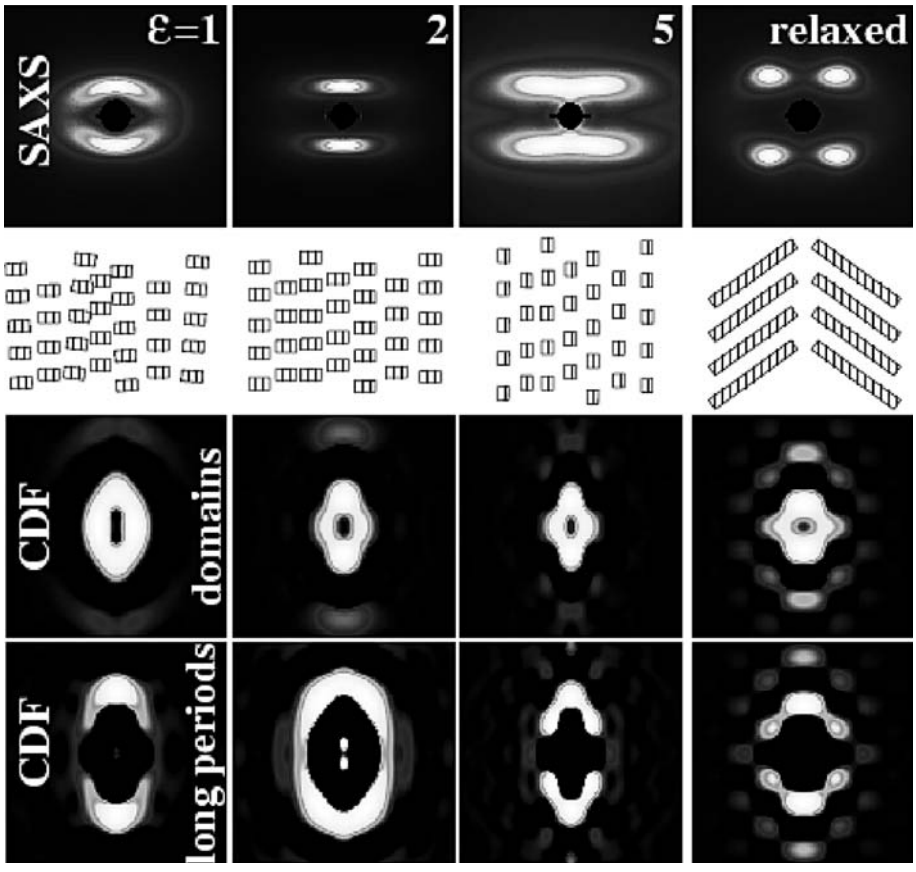

Fig. 2 Straining of a thermoplastic elastomer. Straining direction is vertical. *Top row* SAXS patterns ($-0.25\ nm^{-1}<s_{12},s_3<0.25\ nm^{-1}$), *2nd row* cartoons based on common notions. *3rd* and *4th row* model-free nanostructure information as automatically extracted from the SAXS and presented in real space (chord distribution function, logarithmic intensity scale, $-50\ nm<r_{12},r_3<50\ nm$

lated to the patterns. Ambiguity and possible bias of this method are, in general, conceded.

Some of the shortcomings of this mental pattern inversion are avoided by a computerised inversion such as the one that is described earlier. Practical examples are shown in Fig. 2. In the related study a thermoplastic elastomer was strained. The top row shows the central part of recorded SAXS patterns, underneath cartoons of the nanostructure that are commonly associated to such scattering patterns. The two bottom rows show the chord distribution functions (CDF) computed from the scattering patterns in a "pseudo-colour" representation. In the third row the positive peaks of the CDF are coloured. The bottom row emphasises the negative peaks ("long periods") of the CDFs in real space.

A pattern as observed at an elongation ε=1 is frequently addressed a system of microfibrils with some orientation distribution that are based on cylindrical domains (cf. cartoon). But even lamellar systems with a correlation between layer orientation and long period are discussed. The CDF shows at its "domain face" (third row) that two kinds of domains are present. The stronger peaks are found on the equator. Shape and extension indicate disk-shaped domains oriented parallel to the straining direction (cf. Fig. 3a).

These "lamellae" are thick and their lateral extension is moderate. Two peaks on the meridian indicate a second ensemble of cylindrical domains (cf. Fig. 3b), the height of the latter being close to the diameter of the disks. The discussed peaks only describe the shape of the basic domains but do not carry information concerning the arrangement of neighbouring domains in the matrix. The arrangement of domains is revealed in the peaks from the bottom face of the CDF (Fig. 2, bottom row). At ε=1 the peaks related to the disks are weak. So the lamellae appear to be placed at random in space, although they are rather well oriented. On the other hand, the cylinders form microfibrillar clusters with a long period in the meridional direction. The apparent "ears" of the long period peaks bent towards the equator could be explained by either the aggregation of two slightly tilted layers or by lateral correlations between neighbouring microfibrils ("macrolattice" [44]). The latter explanation appears to be more probable, because a macrolattice based on cylindrical hard

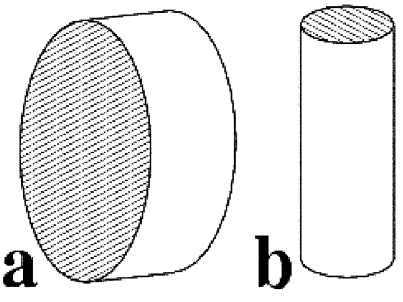

Fig. 3 Sketch of the two domain shapes existing in the strained thermoplastic elastomer, as extracted from the CDFs in Fig. 2. Straining direction is vertical

domains emerges on further elongation. The common cartoon associating a SAXS four-point pattern to stacks of tilted lamellae is thus, in the present case, not describing the correct nanostructure (Fig. 2, right column). The series as a whole exhibits a decrease of the disk fraction and an increase of the cylinder fraction. Quantitative results concerning the fractions and their progression are not available because of insufficient technical setup at beamline A2 (detector, incomplete environmental data). Nevertheless, even the present data suffice for the purpose of quantitatively determining the evolution of domain shape and arrangement during straining.

Example: study the injection moulding of PE

Experimental

High-pressure injection-moulded rods from poly(ethylene) (Lupolen 6021 D, BASF) exhibit a core-shell structure (Fig. 4). In order to achieve high orientation, an equilibrated melt at 160 °C was injected into the cold mould. Maximum mould pressure was 444 MPa and final mould pressure was 336 MPa after 180 s. Samples for the investigation were sectioned from the shell and the core of the rod, respectively, by using a low-speed diamond saw.

Ultra-small-angle X-ray scattering (USAXS) was performed in the synchrotron beamline BW4 at HASYLAB, Hamburg, Germany. USAXS images were collected by a two-dimensional position-sensitive Gabriel detector (512×512 pixels of 0.4×0.4 mm^2) (from European Molecular Biological Laboratory, EMBL). The sample-to-detector distance was set to 12,690 mm.

During image collection, each sample was heated from 25 °C to 150 °C. Below 100 °C a heating rate of 5 °C min^{-1} was chosen. Thereafter the heating rate was slowed to 2 °C min^{-1}. Images were accumulated for 90 s. Data storage took 30 s.

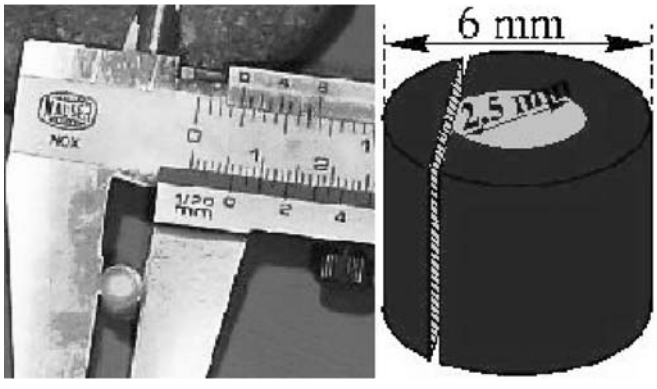

Fig. 4 *Left* PE injection-moulded rod with core–shell structure. *Right* sectioning of a shell sample

Data evaluation

The two-dimensional scattering patterns were normalised to detector efficiency and incident beam flux. Background subtraction and sample absorption were subsequently operated. Blind areas were masked in the images. Each image was centred and aligned using the positions of the observed two-point patterns. Four-quadrant averaging was carried out. The remnant central blind spot from the beam stop was filled. Data for a smooth extrapolation were supplied by radial basis function approximation [45]. The final scattering patterns covered the range $-0.072\ \mathrm{nm}^{-1} < s_1, s_3 < 0.072\ \mathrm{nm}^{-1}$. As described earlier, the scattering intensity was projected onto the (s_1,s_3)-plane, multiplied by s^2, then regridded to 512×512 pixels. The 2D background was determined and subtracted. The result was subjected to 2D Fourier transformation and the 3D chord distribution $z(\mathbf{r})$ was obtained.

Results and discussion

The USAXS patterns

Figure 5 exhibits the logarithm of the USAXS intensity from the shell zone of a high-pressure-moulded PE rod at chosen temperatures during heating of the sample. Sharp long-period reflections with a peak maximum corresponding to 100 nm are obvious in all patterns. The peaks are placed on top of an intensity ridge extending along the meridian. The shape of the ridge changes as a function of increasing temperature, whereas the peak appears to be almost unchanged. The ridge disappears before melting. Equatorial scattering is indicated early at 128 °C. With increasing temperature it becomes more pronounced and vanishes as the last discrete feature when the sample melts.

Figure 6 shows the corresponding USAXS from the core zone of the pressure-moulded PE rod. As compared to the shell zone scattering, we observe more diffuse patterns. But the orientation of the core material is obvious, especially in the pattern recorded at 129 °C. A direct interpretation of these patterns appears to be difficult and ambiguous.

3D chord distributions of the shell material

Figure 7 presents 3D chord distribution functions $z(\mathbf{r})$ of the shell material at various temperatures during heating. It is obvious that a lamellar system is present at ambient temperature. Each of the strong, triangle-shaped peaks in the 3D surfaces describes both crystalline lamellae and amorphous layers. The corresponding layer thickness distributions are broad and cause the corresponding peaks to merge into one. The long period (26 nm) is much smaller than expected from the peak maximum of the scattering pattern.

At 128 °C peak heights have grown. The reason is different thermal expansion of crystalline and amorphous phases, respectively. From the width of the triangles an

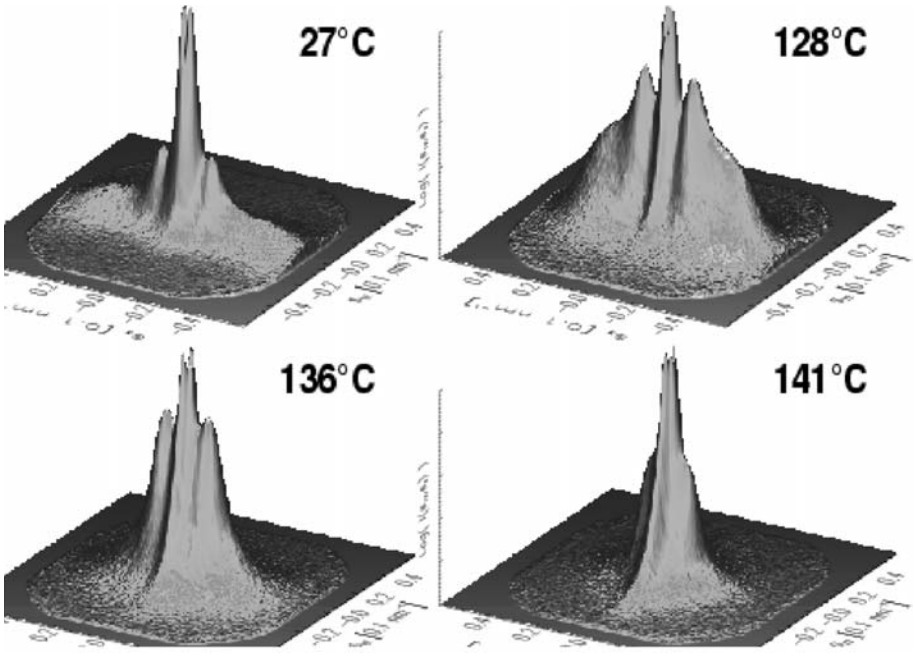

Fig. 5 USAXS intensity log(I(**s**)) from the shell zone of a PE rod at various temperatures during heating

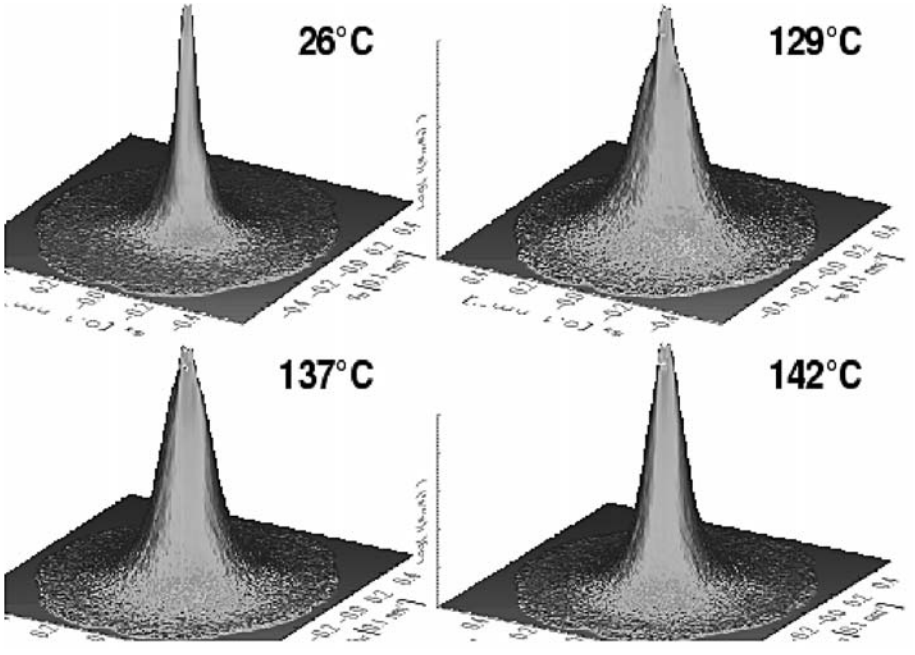

Fig. 6 USAXS intensity log(I(**s**)) from the core zone of a PE rod at various temperatures during heating

average lateral extension of 70 nm is determined. The undulation frequency in front of the strong peaks has halved just as the temperature of 128 °C has been reached. Thus the long period now has doubled. In the centre of the lower peaks of second order an indentation is observed, which is still unexplained at this temperature.

At 136 °C the first minimum in the CDF in the meridional direction (i.e. the long period) is found at 95 nm. The imperfect layers have melted and the only observable feature is the layer stack corresponding to the strong peaks in the scattering pattern. The distribution of layer thicknesses is still very broad. The indentation from the last pattern has increased to form a trough extending along the meridian.

At 141 °C the trough has engraved itself to from a deep valley on the meridian. A more shallow, modulated valley is extending along the equator of the CDF. Single lamellae with a very broad thickness distribution are indicated by the low hills in the pattern.

Minima in the valleys are associated with long periods [13]. In the corresponding contour plots of Fig. 7 it is observed that the long period doubles first at 128 °C and a second time at 136 °C. But still the long equatorial streak indicates the autocorrelation of a lamellar system. At 141 °C the nanostructure has changed fundamentally. The streak at the equator has shrunk to indicate the predominance of domains which are narrow in lateral direction ("blocks").

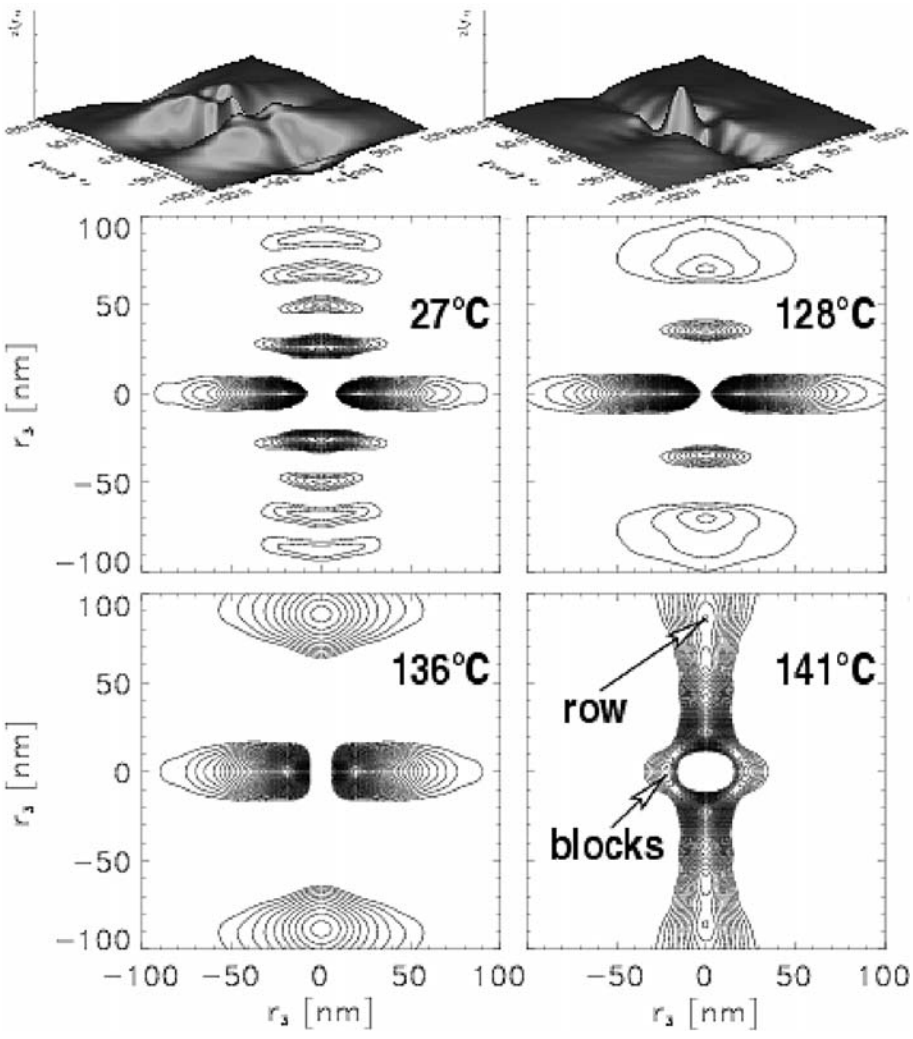

Fig. 7 Shell zone of the PE rod: 3D chord distributions with fibre symmetry, $z(\mathbf{r})$ as a function of temperature during heating in the range $r_3 \in (-100\,\text{nm}, 100\,\text{nm})$. 3D surfaces (*top*) show the function seen from the top. The contour plots *below* show minima ranging downward from the zero level of the function (long periods)

Based on these observation it appears to be justified to assume, to a first approximation, that during heating those crystallites which were formed last during crystallisation are melting first. Let us imagine we reverse time and then discuss the observed process in terms of a crystallisation. Doing so permits us to proceed from the simple to the complex nanostructure. Under this premise the results reveal that upon the start of crystallisation tiny nuclei are forming row structures along the fibre direction. From these nuclei lamellae are growing in the lateral direction. The thicknesses of these lamellae are not uniform (20–60 nm). This result may be caused by the fact that the irradiated volume integrates over the total thickness of the shell zone. During the course of cooling new and thin crystal layers are generated somewhere in between the primary lamellae. When the material is cooled even further, the long period is halved a second time. All the time the most regular period is constant and imprinted by the average distance of the nuclei in the rows. This causes the point-shaped long-period reflections in the scattering pattern. The subdivision of the primary long period in the subsequent insertion crystallisation is highly irregular and generates the intensity ridge extending along the meridian. The strength of the equatorial streak is correlated with the strength of the row structure. Thus the CDF analysis reveals that for the studied materials the insertion model of crystallisation [46, 47] is more probable than the two-stack model [48]. While the scattering pattern is emphasising the harmonic components of the structure, the CDF shows all the regular and irregular components with equal weight and the complexity of the nanostructure is revealed.

Iterated CDFs

In the paper proposing the CDF method [13] a possibility is discussed to remove strong background scattering by iterating the steps of low-pass filter and background subtraction until the values of the CDF vanish in the vicinity of zero. Domain roughness [27, 49] can be compensated this way, but information concerning structure of imperfect domains is lost. From all scattering patterns of the shell material iterated CDFs have been computed and compared to the noniterated ones. The iterated CDFs reproduce the information concerning the fairly well-ordered row structure and the primary lamellae without dis-

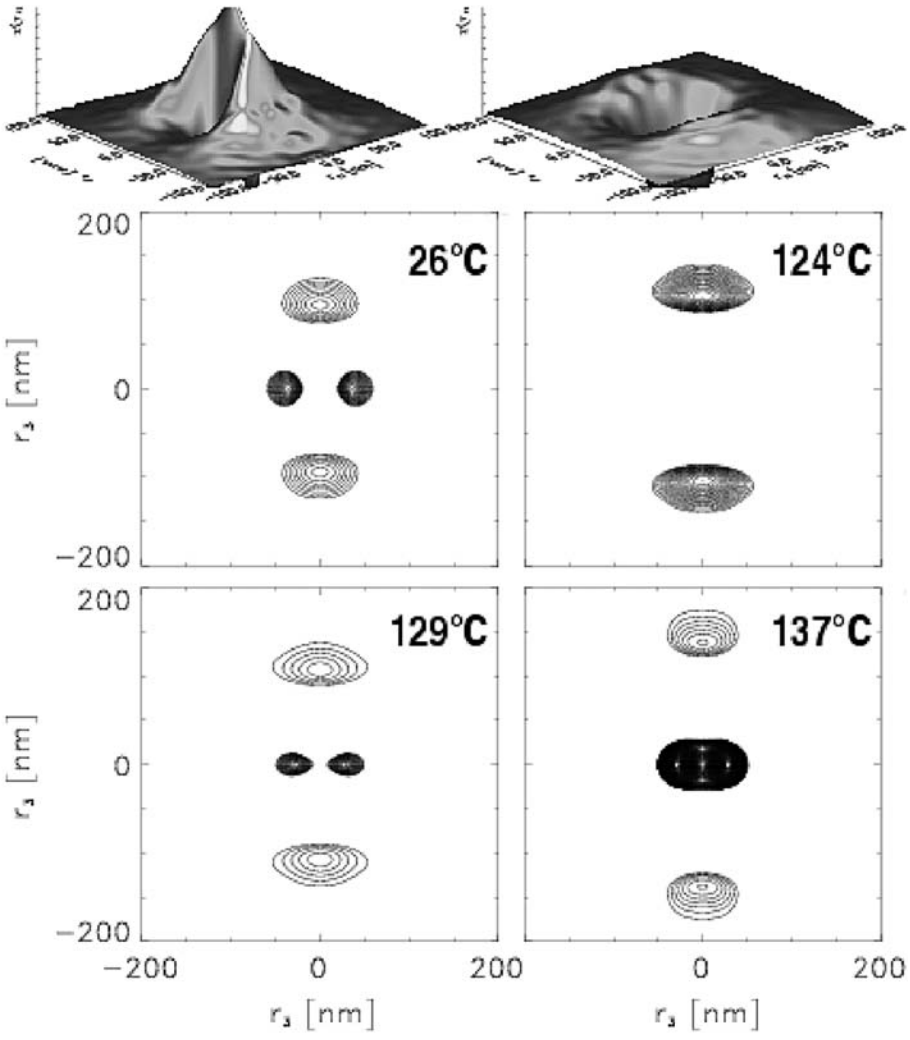

Fig. 8 Core zone of the PE rod: 3D chord distributions with fibre symmetry, $z(\mathbf{r})$ as a function of temperature during heating. 3D surfaces (*top*) show the function seen from the top in the range r_{12}, $r_3 \in (-100\,\text{nm}, 100\,\text{nm})$. The contour plots *below* show minima ranging downward from the zero level of the function (long periods) in the range r_{12}, $r_3 \in (-200\,\text{nm}, 200\,\text{nm})$

tortion. Nevertheless, information concerning the imperfect secondary lamellae is lost.

3D CDF analysis of the core material

Noniterated CDFs from the core zone of the high-pressure-moulded PE rod are shown in the 3D representation of Fig. 8. The nanostructure, in general, exhibits less order as compared to the shell material. At room temperature the long periods are small again and the average extension of the crystallites in the lateral direction is very small as compared to the shell material. A fingerprint of a row structure is not found. At 124 °C the typical triangular peaks from lamellae with some lateral extension are seen. Nevertheless, there are still many irregular domains which are not extended in the lateral direction. At 129 °C it is observed that the average thickness of the remnant lamellae has increased. At 137 °C only a very broad distribution of now very extended lamellae is seen. These findings indicate that even in the core material the insertion model of crystallisation is preferable. The question concerning the existence of a row structure in the core material cannot be answered from the noniterated CDFs.

The contour plots of Fig. 8 show the long periods from iterated CDFs. In contrast to the noniterated CDFs, the iterated CDFs exhibit clear long-period reflections. At room temperature the long period is 95 nm which is the value of the row structure period known from the shell material. Unlike to the finding with the shell material this long period first increases slowly (105 nm at 129 °C), then accelerates up to a value of 140 nm at 137 °C. At higher temperature a regular long period cannot be detected any more.

Obviously the lateral extensions of the domains in the core is lower than in the shell. While the lamellae from the shell exhibit an average cross section of 70 nm, corresponding cross sections in the core material are found between 40 nm and 60 nm.

In summary, even if the ordered structure of both the shell and the core material show the same long period at room temperature the nucleation process is different. In the core material the frame of a uniform row structure is missing. On the other hand, insertion crystallisation is common during the second stage of crystallisation in both the core and the shell material.

Conclusions

The minimal invasive methods that utilise the interaction of synchrotron radiation with material play an important role when processes are studied in situ. The time-resolved SAXS of polymer materials studied during a transformation is not just a powerful tool to investigate the relationship between structure and properties of materials; equally important is the information that can be gained from an analysis of the SAXS concerning the processes that control nanostructure evolution. In the future the enlightenment of such relationships can help to optimise polymer materials with respect to their properties and, beyond that, to improve assessments concerning their aging.

In order to promote this development, the optimisation of synchrotron beamlines with respect to an automated evaluation of voluminous data sets is indicated. One prerequisite for the requested progress is the possibility to collect complete data sets with simple and documented relationships among the patterns. The other prerequisite is the development of evaluation methods that are both suited to deal with multidimensional data sets and that resort to models as late as possible. The evaluation method proposed in this paper is the multidimensional chord distribution analysis. We have exemplified how this method can be utilised to analyse time-resolved studies of nanostructure evolution in materials science. In a similar manner, insight can be gained concerning nanostructure evolution as a function of different kinds of material load. From the nanostructure at ambient temperature and the melting behaviour of materials conclusions can be drawn on processes dominating the preceding crystallisation. We expect that similar investigations will contribute to a deeper understanding of the structure–property relationships of polymers and, finally, to the engineering of tailored polymer materials.

References

1. Grosse-Kunstleve RW, Sauter NK, Moriarty NW, Adams PD (2002) J Appl Cryst 35:126
2. Porod G (1951) Kolloid Z 124:83
3. Glatter O, Kratky O (1982) (eds) Small angle X-ray scattering. Academic Press, London
4. Vonk CG, Kortleve G (1967) Kolloid Z u Z Polymere 220:19
5. Ruland W (1977) Colloid Polym Sci 255:417
6. Förster S, Burger C (1998) Macromolecules 31:879
7. Glatter O (1979) J Appl Cryst 12:166
8. Feigin LA, Svergun DI (1987) Structure analysis by small-angle X-ray and neutron scattering. Plenum Press, New York
9. Vonk CG (1979) Colloid Polym Sci 257:1021
10. Ruland W (1978) Colloid Polym Sci 256:932
11. Stribeck N (1993) Colloid Polym Sci 271:1007
12. Méring J, Tchoubar D (1968) J Appl Cryst 1:153
13. Stribeck N (2001) J Appl Cryst 34:496
14. Bonart R (1966) Kolloid Z u Z Polymere 211:14
15. Stribeck N (1992) Colloid Polym Sci 270:9
16. Stribeck N (1999) J Polym Sci Part B Polym Phys 37:975
17. Stribeck N (2000) ACS Symp Ser 739:41
18. pv–wave Version 7.5 (2001) Visual Numerics, Boulder, Colorado
19. Haberäcker P (1989) Digitale Bildverarbeitung. Hanser, Munich
20. Rosenfeld A, Kak AC (1982) Digital picture processing, vol. 1. Academic Press, London
21. Ruland W (1971) J Appl Cryst 4:70
22. Stribeck N, Ruland W (1978) J Appl Cryst 11:535
23. Fischer L, Haschberger R, Ziegeldorf A, Ruland W (1982) Colloid Polym Sci 260:174
24. Fiedel HW, Wenig W (1989) Colloid Polym Sci 267:369
25. Santa Cruz C, Stribeck N, Zachmann HG, Baltá Calleja FJ (1991) Macromolecules 24:5980
26. Stribeck N, Zachmann HG, Bayer RK, Baltá Calleja FJ (1997) J Mater Sci 32:1639
27. Wolff T, Burger C, Ruland W (1994) Macromolecules 27:3301
28. Stribeck N, Sapoundjieva D, Denchev Z, Apostolov AA, Zachmann HG, Stamm M, Fakirov S (1997) Macromolecules 30: 1329
29. Schmidtke J, Strobl G, Thurn-Albrecht T (1997) Macromolecules 30:5804
30. Stribeck N, Reimers C, Ghioca P, Buzdugan E (1998) J Polym Sci Part B Polym Phys 36:1423
31. Chen HL, Li LJ, Lin TL (1998) Macromolecules 31:2255
32. Thünemann AF, Lochhaas KH (1998) Langmuir 14:6220
33. Heck B, Hugel T, Iijima M, Sadiku E, Strobl G (1999) New J Phys 1:17.1
34. Thünemann AF, Ruland W (2000) Macromolecules 33:2626
35. Iijima M, Strobl G (2000) Macromolecules 33:5204
36. Wutz C, Stribeck N, Gieseler D (2000) Coll Polym Sci 278: 1061
37. Heck B, Hugel T, Iijima M, Strobl G (2000) Polymer 41:8839
38. Flores A, Pietkiewicz D, Stribeck N, Roslaniec Z, Baltá Calleja FJ (2001) Macromolecules 34:8094
39. Fu Q, Heck B, Strobl G, Thomann Y (2001) Macromolecules 34:2502
40. Hsiao BS, Verma RK (1998) J Synchrotron Radiat 5:23
41. Stribeck N (2002) Colloid Polym Sci 280:254
42. Fakirov S (1985) Bulg J Phys 2:173
43. Stribeck N (1997) Fibre Diffraction Rev 6:20
44. Fronk W, Wilke W (1985) Colloid Polym Sci 263:97
45. Buhmann MD (2000) Acta Numerica 9:1
46. Wang J, Alvarez M, Zhang W, Wu Z, Li Y, Chu B (1992) Macromolecules 25:6943
47. Hsiao BS, Gardner KH, Wu DQ, Chu B (1993) Polymer 34: 3996
48. Bassett DC, Olley RH, Al Raheil IAM (1988) Polymer 29:1745
49. Ruland W (1987) Macromolecules 20:87